Université Scientifique et Médicale de Grenoble

INSTITUT DES SCIENCES NUCLÉAIRES
DE GRENOBLE

53, avenue des Martyrs - GRENOBLE

ISN 80.31
July 1980

DEEPLY INELASTIC COLLISIONS AND FUSION IN THE $^{20}Ne + ^{40}Ca$ SYSTEM

NGUYEN VAN SEN, J.C. GONDRAND, F. MERCHEZ and R. DAVIES-BLANC

Submitted for publication

Laboratoire associé à l'Institut National de Physique Nucléaire et de Physique des Particules.

DEEPLY INELASTIC COLLISIONS AND FUSION IN THE $^{20}Ne + ^{40}Ca$ SYSTEM

Nguyen Van Sen, J.C. Gondrand, F. Merchez and R. Darves-Blanc
Institut des Sciences Nucléaires, IN2P3 and USMG, 38026 Grenoble, France

Cross sections for deeply inelastic collisions, fusion, and elastic scattering of ^{20}Ne on ^{40}Ca were measured at 151 MeV. The critical angular momentum L_{cr} and the grazing one L_{gr} deduced from the fusion and elastic scattering data were used in an attempt to interpret the fragment kinetic energies in deeply inelastic collisions in terms of a rotating double-nucleus system whose contributing initial angular momentum depends explicitly on the amount of nucleon transfer.

[NUCLEAR REACTIONS $^{20}Ne + ^{40}Ca$, E = 151 MeV, measured energy spectra, angular distributions for $4 \leq Z \leq 15$, elastic scattering angular distribution, evaporation residue cross section. Gas ionization and Si detectors. Natural target. Deduced optical model parameters, reaction cross section, fragment kinetic energies.]

I. INTRODUCTION

Since the discovery of the deeply inelastic transfer reactions in heavy-ion collisions, many experimental and theoretical studies have been performed in order to understand the main features of this type of reaction, which combines properties characteristic of two apparently opposite nuclear processes : direct reaction and compound nucleus decay[1]. These properties are believed to derive from the formation of a double-nucleus composite system in the early stage of the reaction. The major part of previous studies[1,2] has been preferably devoted to heavy systems involving projectiles larger than Ar and heavier targets. In a very heavy system the strong Coulomb repulsion prevents the evolution of the double-nucleus system toward fusion for most values of the orbital angular momentum, so that the deeply inelastic processes account for a predominant part of the total reaction cross section. Furthermore, reactions between heavy complex nuclei are more suitable to an interpretation in terms of classical concepts and statistical mechanisms[3]. A typical example of such studies has been fully described by Schröder et al. [3] for the Xe + Bi system.

The deeply inelastic collisions involving composite systems with mass numbers ranging from about 50 to 100 exhibit many features similar to those found in reactions studied with heavy systems,[4,5] however several particular characteristics have been obtained. On light systems, the centrifugal barrier is comparable to the Coulomb one, and the rotation of the composite system plays then a significant role, so that the experimental data provide useful informations on the deformation of a rapidly rotating double nucleus system before scission[5,9]. Besides, direct reaction characteristics become more conspicuous. For example, a good description of the energy spectra of the reaction products could be recently obtained through quantum mechanical treatments and a microscopic picture assuming direct transfer and break-up processes[10,11]. Previous studies of the deeply inelastic collisions involving projectiles lighter than Ar and medium-weight targets include $^{35}Cl + ^{27}Al$ at 140 to 170 MeV,[8-12] $^{32}S + ^{50}Ti$ at 105 to 166 MeV,[13-15] ^{20}Ne + Ni at 164 MeV[4], and $^{20}Ne + ^{27}Al$ at 120 MeV.[5]

In the present work, the system $^{20}Ne + ^{40}Ca$ was investigated at 151 MeV. Simple classical calculations using the phenomenological potentials obtained previously [16] in the description of fusion and elastic scattering data for the same system at 44-70 MeV predict that at 151 MeV the fusion cross section represents about half of the total reaction cross section. The deeply inelastic components are then expected to have comfortable yields centered around the projectile and well separated from the fusion products. The system chosen permits thus to study the deeply inelastic reaction simultaneously with the fusion. With a gas-flow ionization chamber , the heavy fragments either from the fusion process or the deeply inelastic collisions were detected, and angular distributions were obtained. The elastic scattering angular distribution was also measured. The critical L_{cr} and the grazing L_{gr} angular momenta deduced respectively from the fusion and the elastic scattering data were used in an interpretation of the total fragment kinetic energies in terms of a rotating double-nucleus system.

II. EXPERIMENTAL PROCEDURE

The experiment was performed with the 151 MeV ^{20}Ne (6^+) beam from the Grenoble isochronous cyclotron. Self-supporting natural Ca targets were placed at the center of an 1 m diam. scattering chamber. Thicknesses of 100 $\mu g/cm^2$ were used for the fusion measurements instead of 200 and 500 $\mu g/cm^2$ for the deep inelastic measurements. The targets were always protected from oxydation by vacuum or argon atmosphere. A collimator composed of three successive tantalum slits limited the focused beam spot at the target position to about 3 mm in diameter. Beam intensities from 0.1 to 25 electric nA were collected during the measurements by a Faraday cup placed downstream of the scattering chamber.

The heavy fragments were detected by means of an ionization chamber run with a mixture of 90% Ar + 10% CH_4 gas at constant pressures. Low pressures corresponding to about 200 $\mu g/cm^2$ ΔE gas detector were used for the fusion measurements whereas pressures about four times higher were used for the deep inelastic experiments. The ionization chamber contains two low-resistivity Si surface-barrier detectors on its internal rear side. Two simultaneous E-ΔE spectra could thus be obtained for two angles separated by 4° lab.. The solid angle of the ΔE counters was limited to about 0.1 msr in order to permit accurate measurements at small forward angles and to account for the multiple scattering. The angular uncertainty on the detection angle was about ± 0.05° A Parylen-C (Ref. 17) entrance window, 0.3 μm thick, was used for the ionization chamber.

Measurements of the elastic scattering cross section were made at the same time by means of Si detector telescopes mounted on the opposite side of the beam direction. A Si monitor detector was placed at a fixed forward angle in order to obtain the relative normalization of the yield for either the ionization chamber or the elastic scattering telescopes. The absolute normalization for the elastic scattering cross section were obtained by assuming a Rutherford value at the most forward measured angle. The accuracy of this procedure was checked with conventional optical model calculations. The absolute normalization for the cross section of the fragments detected in the ionization chamber was

obtained by comparing the fragment yield to the elastic counts within the same ΔE-E combination.

The pulses from the detectors were processed by conventional electronics and forwarded event by event to a PDP-9 computer through a multiplexor circuitry and an analogic-digital converter. The events were stored on magnetic tapes. The data reduction was performed off-line on PDP and CDC-7600 computers. The overview of the two-dimensional E vs. ΔE spectra obtained from the ionization chamber run with low gas pressure is similar to that shown in Ref. 16, with however a larger yield for the projectile-like fragments. The evaporation residues from the Zn compound-nucleus decay are still well separated from the light transfer reaction products concentrated around the projectile line. The fusion yield could be obtained by counting the events inside a software contour around the evaporation residue mountain.

The yield for the quasi-elastic and deeply inelastic processes was measured by running the ionization chamber with high pressure corresponding to about 0.8 mg/cm^2 ΔE gas detector, where elemental lines are obtained with a $\Delta Z \approx 0.3$ resolution. The energy spectra for each individual Z could be deduced by a software transformation of the E vs. ΔE representation into the energy E_{tot} vs. Z representation, where $E_{tot} \approx E + \Delta E + \delta E$ with δE being a correction term. This correction was made for each E-ΔE combination by taking into account the energy losses in the target, the Parylen entrance window of the ionization chamber and the dead layer of the Si detector by means of the Northcliffe and Schilling stopping powers[18]. Pulse-height defects for heavy ions in the Si surface-barrier detector were also corrected using the methods in Refs. 19 and 20. From the E_{tot} vs. Z representation, the energy spectrum for each individual element, and the total energy-integrated Z distribution within selected energy windows could be obtained for each measured angle. Two typical energy-integrated Z distributions are shown in Fig. 1 where the elemental separation is obtained for fragments from Be to P. The elemental separation is actually improved whenever an energy selection is used.

III. EXPERIMENTAL RESULTS

The fusion angular distribution were measured from 4° to 24° lab.. In order to obtain the angle-integrated cross section σ_{fus}, the angular distribution was extrapolated into the 0°-4° region not measured by fitting the data in the range 0°-8° with the equation

$$d\sigma_{fus}/d\Omega = a\sin^2\theta + b. \qquad (1)$$

This form is roughly consistent with the statistical model calculations.[16,21] The σ_{fus} is actually obtained by finding the area under the curve $d\sigma_{fus}/d\theta$ vs. θ shown in Fig.2, so that the uncertainty due to the extrapolation procedure is less than a few percent. The integrated cross section is σ_{fus} = 995 ± 50 mb, where the uncertainty takes into account the statistical uncertainty, the absolute normalization, and extrapolation procedure errors. The elastic scattering angular distribution measured from 4° to 30° lab. is plotted in Fig. 3. The errors are about ± 5% including statistical and background subtraction uncertainties (±3%), and absolute normalization errors (± 3%). The angular accuracy is about ± 0.05° and the ^{20}Ne beam energy is 151 ± 1 MeV.

Energy spectra from 8° to 64° were obtained for fragments with Z = 4 to 15. Most of the spectra present a bell-shaped distribution corresponding to a strongly damped process. At backward angles and/or for the fragments far from the projectile these distributions are nearly symmetrical about the maximum energy. But for the fragments near the projectile, the distributions at forward angles are more dissymmetrical with a longer low-energy tail. Some typical spectra are shown in Fig. 4, where it is noticeable that at 40° lab. the distribution width is nearly independent of the detected fragment while at 20° lab. the distributions for fragments near the projectile, such as O, F, Na, are much broader than for the lighter and heavier fragments. A bell-shaped structure could not be clearly observed for the Ne fragment at angles smaller than 20° because essentially of the elastic scattering yield, the low-energy background, the increasing contribution from inelastic scatterings and quasi-elastic components, and also of the decreasing energy separation between the elastic peak and the strongly damped component.

For each measured angle, the cross section of the energy-integrated bell-shaped distributions, plotted in function of the fragment charge Z as in Fig. 5, present a clear odd-even effect. The angular distributions obtained for each indivual fragment are shown in Fig. 6. These distributions are more and more forward peaking when the transferred nucleon number decreases. The slope change at about 36° lab. and an interference like structure are not at variance with the assumption of two components : a fast interaction time component at forward angle and a fully relaxed component at backward angle. Such an assumption is also supported by the angular behavior of the total kinetic energy E_F calculated for the centroid of the bell-shaped structure using two body kinematics. Some typical E_F data are shown in Fig. 7. For fragments near the projectile, E_F decreases when the angle increases up to about 36° lab, then attains a nearly constant value beyond this angle suggesting a decay from a fully equilibrated system. It is notable in Fig. 6 that the angular distributions at backward angles are fairly close to the dashed curves corresponding to an $1/\sin\theta$ distribution in the center-of-mass ; such a feature is also indicative of equilibrium processes.

The total elemental yields were obtained by integrating over angle the $d\sigma/d\theta_{lab}$ deduced from the angular distributions shown in Fig.6. The $d\sigma/d\theta_{lab}$ data were extrapolated into the forward angular range not measured by a smooth hand-drawn continuation. For the Ne fragment, the data at angles less than 20° were tentatively obtained by interpolation between the distributions for F and Na ; such an interpolation is assumed in light of the forward angle distributions similarity for those fragments. The angle-integrated elemental yields are plotted in Fig. 8, where the error bars take into account the statistics uncertainty and the extrapolation procedure errors.

In order to obtain an overview of the complete Z distribution of the $^{20}Ne + ^{40}Ca$ reaction studied, the evaporation residue part of spectra deduced from low gas-pressure measurements was tentatively converted into a fusion Z distribution. Although the resolution of the ionization chamber did not permit an individual identification of the

evaporation residue, careful calibrations of the spectra and a simultaneous fitting of the light transfer products and the heavy evaporation residues allow one to deduce a rough Z distribution for each measured angle. These distributions were then integrated over angle by the same procedure as for the total fusion cross section. The evaporation residue Z distribution so obtained is in qualitative agreement with standard evaporation calculations using the ALICE code[22] ; the shift of the experimental distribution towards lower Z values by about two units as shown in Fig. 8 may be understood in terms of angular momentum effects not taken into account in the simple calculations performed. It is notable in Fig. 8 that there is no appreciable ambiguity for separating the deeply inelastic component from the evaporation part ; and that the total deeply inelastic cross section, σ_{DI} = 1010 ± 100 mb are comparable with the fusion cross section σ_{fus} = 995 ± 50 mb. The σ_{DI} cross section so obtained includes actually some contributions from the quasi-elastic collisions particularly at forward angles where the deeply inelastic component cannot be unambiguously resolved from the quasi-elastic component.

IV - THEORETICAL ANALYSIS

A. Elastic scattering

The elastic scattering angular distribution was analyzed in terms of the optical model. Calculations were performed with the SPI code[23] using a four-parameter potential

$$U(r) = V_{coul} - \frac{(V + iW)}{1 + \exp\left\{\left[r - r_o(A_p^{1/3} + A_T^{1/3})\right]/a\right\}} \qquad (2)$$

where V_{coul} is the Coulomb potential for a uniformly charged sphere of the same radius as the complex nuclear part.

The determination of the nuclear potential strength V by fitting the elastic data is actually subject to ambiguities, so that V could be fixed arbitrarily. Similarly with a previous work[16] on ^{20}Ne + ^{40}Ca at 44-70 MeV, V is postulated to have the strength deduced from the liquid drop model by Siwek-Wilczynska and Wilczynki[24]

$$V = b_{surf} \left[A_p^{2/3} + A_T^{2/3} - (A_p + A_T)^{2/3} \right],$$

where $b_{surf} \approx 17$ MeV is the surface energy parameter. For the system studied V = 63.54 MeV. It has been shown at lower energies[16] that when this strength is used, the interaction barrier characteristics deduced from the real part of the best-fit optical potential were comparable with that deduced from the fusion data through various models.

The strength V being fixed, a gridding search was made for the imaginary depth W. For a chosen value of W in the range 0-63 MeV the χ^2 minimization was performed by adjusting r_o and a. The best-fit shown in Fig. 3 was obtained with W = 40 MeV, r_o = 1.162 fm, and a = 0.681 fm. The calculated total reaction cross section is then σ_R = 2158 mb ; this value is close to the sum of the measured fusion cross section σ_{fus}, and deeply inelastic and quasi-elastic cross section σ_{DI}.

The elastic scattering cross section in Fig. 3 falls off to $\frac{1}{4}$ of the Rutherford value at $\theta_{1/4} = 20.0 \pm 0.5°$. With the classical Blair recipe[25], the grazing angular momentum can be deduced through the relationship

$$\ell_{gr} \approx \ell_{1/4} = \eta \cot (\theta_{1/4}/2), \qquad (4)$$

where η is the Sommerfeld parameter ; and the total cross section is then

$$\sigma_R^{(1/4)} = \pi \lambda^2 (\ell_{gr} + 1)^2, \qquad (5)$$

where λ is the reduced wave-length. For the present data, ℓ_{gr} = 65 and $\sigma_R^{(1/4)}$ = 2131 mb. These values are consistent with the optical model calculations. With a similar sharp-cutoff relationship as in Eq. (5) the critical angular momentum can be deduced from the measured

fusion cross section ; $\ell_{cr} = 44$. This value is consistent with that deduced from the real part of the best-fit optical potential by defining ℓ_{cr} as the angular momentum for which the projectile just surmounts the barrier provided by the sum of the Coulomb and centrifugal potentials and the real nuclear potential. In fact, no minimum in the total potential energy and then no fusion barrier occurred for partial waves with $\ell > 44$, so that the critical angular momentum attained a saturated value $\ell_{cr} = 44$. The same result was obtained with the proximity potential of Blocki et al [26], using the original parameters except for the radius which is chosen to be

$$R_i = r_o A_i^{1/3} - 0.76 + 0.8 A_i^{-1/3} \text{ fm}, \qquad (6)$$

with $r_o = 1.37$ fm instead of 1.28 fm as suggested in ref. 26. Such an increase has been necessary in order to fit the fusion data at lower energies [16].

B. Deeply inelastic reactions

The rotation-energy contributions to the kinetic energies of deeply-inelastic reaction products from light heavy-ion systems have been the subject of several studies [5-9, 27]. The colliding nuclei are assumed to form a double-nucleus system, whose final configuration was a pair of sticking rotating fragments. The scission configuration may be approximately described by two uniform spheres of radii R_3 and R_4 joined by a thin neck. The distance between the mass centers of the two fragments is then given by

$$d = R_3 + R_4 + \delta \qquad (7)$$

where δ is the length of the neck, and R_i can be taken to be $R_i = 1.2 A_i^{1/3}$.

Taking into account the frictional force, the total kinetic energy of the rotating double-nucleus system is given by

$$E_F = V_{Coul}(d) + V_{nucl}(d) + f^2 \frac{L_i(L_i+1)\hbar^2}{2\mu d^2} \qquad (8)$$

where

$$f = \mu d^2/(\mu d^2 + \mathcal{J}_3 + \mathcal{J}_4)$$

$$\mathcal{J}_i = \frac{2}{5} m_i R_i^2 ,$$

μ being the reduced mass and m_i the fragment masses. In previous works[5-9], the rotational energy has been deduced from the measured fragment kinetic energy by assuming a fixed angular momentum L_i for any detected fragment. The partial wave L_i is chosen to be the wave just greater than those going to fusion, or the one midway between fusion and grazing. It might be more reasonable to assume that L_i depends on the amount of nucleon transfer which should depend on the initial impact parameter and then on the degree of overlap between the interacting nuclei in the initial stage of the reaction [27]. Since the nuclear potential is small compared to the Coulomb potential and the rotation term, one may consider the amount of proton transfer instead of the nucleon transfer. For small numbers of transferred protons the smallest degree of nuclear overlap is expected, so that these reactions are associated with large impact parameter and are then dominated by contributions from partial waves near the grazing L_{gr}. On the contrary the partial waves just larger than the critical L_{cr} correspond to small impact parameters and large nuclear overlap giving rise to large proton transfers. It may be thus assumed [27] that deeply-inelastic transfer reaction is associated with a small number of partial waves centered at

$$L_i = \alpha L_{cr} + (1 - \alpha) L_{gr}, \qquad (9)$$

where α accounts for the degree of nuclear overlap.

With the assumption that the proton transfer is proportional to the volume of one of the interacting nuclei which is swept by the other nucleus, Simbel and Abul-Magd [27] have shown that

$$\alpha = |n|/n_{max} \qquad (10)$$

where n is the number of transferred protons, and n_{max} is the maximum of this number corresponding to a maximum overlap and then to the initial angular momentum equal to L_{cr}. If it is assumed further that L_{cr}

corresponds to an overlap at the critical distance [28]

$$R_{cr} = 1.0\ (A_1^{1/3} + A_2^{1/3})\ \text{fm} \qquad (11)$$

and that the grazing occurs at

$$D = 1.5\ (A_1^{1/3} + A_2^{1/3})\ \text{fm}, \qquad (12)$$

n_{max} is approximately [27]

$$n_{max} \simeq \frac{Z_1}{12}\left[1 + \left(\frac{A_2}{A_1}\right)^{1/3}\right]^2 \qquad (13)$$

Beside the angular momentum L_i, the extraction of the rotational energy from the fragment kinetic energy requires also the knowledge of the distance d and the nuclear potential at this distance. Actually Eq. (8) can be satisfied either by a solution with d much larger than the nuclear radii so that the nuclear potential is practically negligible or by a solution with d comparable to the nuclear radii where the attractive nuclear potential should be taken into account in order to compensate the increases of the Coulomb and rotational parts.

In the present work, the initial angular momentum L_i was calculated through Eq. (9) with L_{cr} and L_{gr} precedingly deduced from the fusion and elastic scattering data, $L_{cr} = 44$ and $L_{gr} = 65$. The nuclear potential in Eq. (8) was taken to be the proximity potential [26] used with the radius modified as in Eq. (6) ; the mass and charge dependence of the nuclear potential is then accounted for in the determination of proximity potential parameters [26]. It was assumed that the fragment mass is twice its charge. A point-charge potential was used for the Coulomb part $V_{Coul}(d) = Z_3 Z_4\ e^2/d$. The only parameter to be varied in the calculations of the total kinetic energies E_F was then the neck length δ defined in Eq. (7).

A good overall description of the E_F data at the grazing angle $\theta_{gr} = 20°$ lab. could be obtained as shown in Fig.9, with $\delta = 6.3$ fm. There is a noticeable shift between the experimental distribution centered around Z = 8-9 and the model prediction which has a maximum at the pro-

jectile charge Z = 10. This shift is understandable in terms of light particle evaporations by the excited fragments prior to the experimental detection. In order to take into account the kinetic energy lost by the fragments in the evaporation processes, the measured E_F should be roughly corrected by a factor 1 + (n/A) where A is the composite system mass and n is the number of evaporated nucleons [29]. The best-fit neck length δ should then decrease by a few percent, but is still appreciably larger than the $\delta \simeq 2$ fm used in analyses of fission data [30]. The large δ obtained, in agreement with previous results,[27] is indicative of the high deformation of the residual nuclei at scission.

For detection angles much larger than the grazing one, the deeply inelastic collision is assumed to be associated with a small impact parameter, and thus with contributions from partial waves just larger than the critical one. Calculations made with $L_i = L_{cr} + 1 = 45$ and $\delta = 0$ could fairly reproduce not only the E_F data measured at 40° lab. as shown in Fig. 9 but also those measured at larger angles, since E_F attains in Fig. 7 nearly constant values beyond 36° lab.. In these calculations, no dependence on the number of transferred protons was assumed and L_i was kept fixed for all fragments.

The results obtained suggest that the two solutions of Eq.(8) correspond to two physical components. The solution with large d and with L_i explicitly dependent on the number of transferred protons is associated with deeply inelastic products detected around the grazing angle while the more damped products detected at much larger angles are described by the solution with small d and L_i just larger than L_{cr} independently of the amount of proton transfer.

The crude model used is not expected to be valid for the data at angles forward of the grazing, where the spectra may be dominated by direct-reaction processes particularly for the fragments near the projectile. Several mechanisms have been investigated, for example projectile fragmentation [31,32], transfer reaction and projectile breakup [10,11,33].

In particular the reaction ^{40}Ca (^{20}Ne, ^{16}O) has been studied at 262 and 149 MeV for the forward angles. The ^{16}O spectra could be reproduced by distorted-wave-Born-approximation calculations assuming both a transfer and a breakup process : the ^{16}O dissymmetrical spectra were constructed by summing two components, a breakup component centered around the beam velocity, and a transfer component occurring at lower energy. The breakup component decreases rapidly in function of angle and becomes negligible at angles backward of the grazing one so that the spectra have then a more symmetrical shape. The forward angles O data of the present work are in agreement with those obtained for ^{16}O in Refs. 10 and 11, whereas the fragments far from the projectile, for example N and C have nearly symmetrical bell-shaped distributions similar to spectra obtained at larger angles, shown in Fig.4, suggesting no evidence for a breakup contribution. Analyzing the data at the most forward angles is beyond the scope of the present work ; promising results have been obtained in attempts to understand the evolution from the simple direct transfer or breakup reaction towards the deeply inelastic collision [10,11,33].

V. CONCLUSION

Cross sections for the deeply inelastic collisions of ^{20}Ne on ^{40}Ca were measured at 151 MeV by detecting fragments from Be to S with a gas-flow ionization chamber. Most of the spectra present a bell-shaped distribution corresponding to a strongly damped process. The angular distributions for individual fragments are more forward peaking for the fragments with charges near that of the projectile than for the lighter and heavier fragments. The angular behavior of the cross sections and of the total kinetic energy of the exit channel are not at variance with the assumption of a fast interaction time component at forward angles and a relaxed component at angles larger than about 36° lab.. The total cross section for the deeply inelastic and quasi-elastic collisions is practically equal to the complete fusion cross section. The fusion measurements were made by detecting the evaporation residues from the Zn compound nucleus decay with the same ionization chamber run at low gas pressure. The elastic scattering angular distribution was also measured with solid state detectors.

From the elastic scattering data, the grazing angle θ_{gr} and angular momentum L_{gr} were deduced whereas the critical angular momentum L_{cr} was obtained from the fusion data by means of classical approximations. The L_{cr} and L_{gr} angular momenta were used in an attempt to interpret the total kinetic energy E_F in terms of a rotating double-nucleus system. A good overall description of the E_F data at the grazing angle, $\theta_{gr} = 20°$ lab, could be obtained by using a neck length appreciably larger than the value employed in previous fission analyses, and by taking into account an explicit dependence of the initial angular momentum L_i of the colliding system on the amount of proton transfer. For detection angles much larger the grazing one, the E_F data are better described by calculations with a small neck length and no explicit dependence on the amount of proton transfer, L_i is being kept fixed to the value just larger than L_{cr}.

The authors wish to thank A. MAURICE for technical assistance and J.P. RICHAUD for target preparation.

REFERENCES

[1] V.V. Volkov, Phys. Rep. 44, 93 (1978) and references therein.

[2] W.U. Schröder and J.R. Huizenga, Ann. Rev. Nucl. Sci. 27, 465 (1977) and references therein.

[3] W.U. Schröder, J.R. Birkelund, J.R. Huizenga, K.L. Wolf, and V.E. Viola, Jr., Phys. Rep. 45, 301 (1978).

[4] F.E. Obenshain, R.L. Ferguson, H.L. Halbert, D.C. Hensley, H. Nakahara, F. Plasil, F. Pleasonton, A.H. Snell and R.G. Stokstad, Phys. Rev. C18, 764 (1978).

[5] J.B. Natowitz, M.N. Namboodiri, R. Eggers, P. Gonthier, K. Geoffroy, R. Hanus, C. Towsley and K. Das, Nucl. Phys. A277, 477 (1977).

[6] R. Eggers, M.N. Namboodiri, P. Gonthier, K. Geoffroy, and J.B. Natowitz, Phys. Rev. Lett. 37, 324 (1976).

[7] P. Braun-Munzinger, T.M. Cormier, and C.K. Gelbke, Phys. Rev. Lett. 37, 1582 (1976).

[8] T.M. Cormier, P. Braun-Munzinger, P.M. Cormier, J.W. Harris, and L.L. Lee, Jr., Phys. Rev. C16, 215 (1977).

[9] R.R. Betts and S.B. DiCenzo, Phys. Rev. C19, 2070 (1979).

[10] H. Fröhlich, T. Shimoda, M. Ishihara, K. Nagatani, T. Udagawa, and T. Tamura, Phys. Rev. Lett. 23, 1518 (1979).

[11] K. Nagatani, in Proceedings of the Symposium on Heavy Ion Physics from 10 to 200 MeV/amu, Brookhaven National Lab., 1979, edited by J. Barrette and P.D. Bond, Vol. 2, p. 833.

[12] T.M. Cormier, E.R. Cosman, A.J. Lazzarini, J.D. Garrett, and H.E. Wegner, Phys. Rev. C14, 127 (1976).

[13] J. Barrette, P. Braun-Munzinger, C.K. Gelbke, E. Grosse, H.L. Harney, J. Krominski, I. Tserruya, and Th. Walcher, Z. Phys. A274, 121 (1975).

[14] P. Braun-Munzinger, C.K. Gelbke, J. Barrette, B. Zeidman, M.J. Levine, A. Gamp, H.L. Harney and Th. Walcher, Phys. Rev. Lett. 36, 849 (1976).

[15] C.K. Gelbke, P. Braun-Munzinger, J. Barrette, B. Zeidman, M.J. Levine, A. Gamp, H.L. Harney and Th. Walcher, Nucl. Phys. A269, 460 (1976).

[16] Nguyen Van Sen, R. Darves-Blanc, J.C. Gondrand, and F. Merchez, Phys. Rev. C20, 969 (1979).

[17] Manufactured by Union Carbide Corporation.

[18] L.C. Northcliffe and R.F. Schilling, Nucl. Data Tables A7, 233 (1970).

[19] A.J. Gorski and M.J. Fluss, Nucl. Instrum. Methods 115, 47 (1974).

[20] J.B. Moulton, J.E. Stephenson, R.P. Schmitt, and G.J. Wozniak, Nucl. Instrum. Methods, 157, 325 (1978).

[21] Y. Eyal, M. Beckerman, R. Chechik, Z. Fraenkel, and H. Stocker, Phys. Rev. C13, 1527 (1976).

[22] M. Blann, ALICE : A Nuclear Evaporation Code, Univ. of Rochester, N.Y., Report COO-3494-19.

[23] F.G. Perey, Phys. Rev. 131, 745 (1963) and private communication

[24] K. Siwek-Wilczynska and J. Wilczynski, Phys. Lett. 74B, 313 (1978) ; 55B, 270 (1975).

[25] J.S. Blair, Phys. Rev. 108, 827 (1957).

[26] J. Blocki, J. Randrup, W.J. Swiatecki and C.F. Tsang, Ann. Phys. (N.Y.) 105, 427 (1977).

[27] M.H. Simbel and A.Y. Abul-Magd, Z. Physik A294, 277 (1980).

[28] J. Galin, D. Guerreau, M. Lefort and X. Tarrago, Phys. Rev. C9, 1018 (1974).

[29] P. Wastyn, H. Feldmeier, F. Beck, M. Dworzecka, H. Genz, M. Mutterer, A. Richter, G. Schrieder, and J.P. Theobald, Nucl. Phys. A332, 455 (1979).

[30] K.T.R. Davies, A.J. Sierk, and J.R. Nix, Phys. Rev. C13, 2385 (1976).

[31] A.S. Goldhaber, Phys. Lett. 53B (1974) 306.

[32] C.K. Gelbke, D.K. Scott, M. Bini, D.L. Hendrie, J.L. Laville, J. Mahoney, M.C. Mermaz, and C. Olmer, Phys. Lett. 70B, 415 (1977).

[33] K.W. McVoy and M.C. Nemes, Z. Physik, A295, 177 (1980).

FIGURE CAPTIONS

Fig. 1 - Energy-integrated elemental yields deduced from the ionization chamber E vs. ΔE two-dimensional spectra.

Fig. 2 - Angular distribution of the evaporation residue cross section for $^{20}Ne + ^{40}Ca$ at 151 MeV. The total fusion cross section σ_{fus} is obtained by integrating over angle the solid curve. The 0° - 4° part is deduced from the extrapolation procedure performed on the $d\sigma_{fus}/d\Omega$ angular distribution (see text).

Fig. 3 - Elastic scattering angular distribution for $^{20}Ne + ^{40}Ca$ at 151 MeV, compared with the best-fit optical model calculations using a four-parameter complex potential.

Fig. 4 - Experimental spectra at 20° and 40° lab. for fragments from Be to S. The dashed lines are drawn to guide the eye. The bell-shaped distribution FWHM is indicated by a horizontal full line segment.

Fig. 5 - Elemental differential cross sections showing odd-even effects.

Fig. 6 - Angular distributi .s of the deeply inelastic bell-shaped part of the spectra. The dashed curves are deduced from an $1/\sin \theta_{cm}$ angular distribution in the center-of-mass, using two-body kinematics and the most probable Q-values of deeply inelastic component ; the curves are normalized to the data at backward angles.

Fig. 7 - Total kinetic energies of the fragment exit channel in the center of mass system.

Fig. 8 - Energy and angle integrated elemental cross section for fragments and evaporation residues produced in the $^{20}Ne + ^{40}Ca$ at 151 MeV. The full line is drawn to guide the eye through the measured data. The dashed line represents the evaporation residue distribution calculated with the ALICE code [22], the calculations are normalized so as to provide the same Z-integrated fusion cross section as the experimental data.

Fig. 9 - Total kinetic energies of the fragments compared with calculations based on a rotating double-nucleus model (see text).

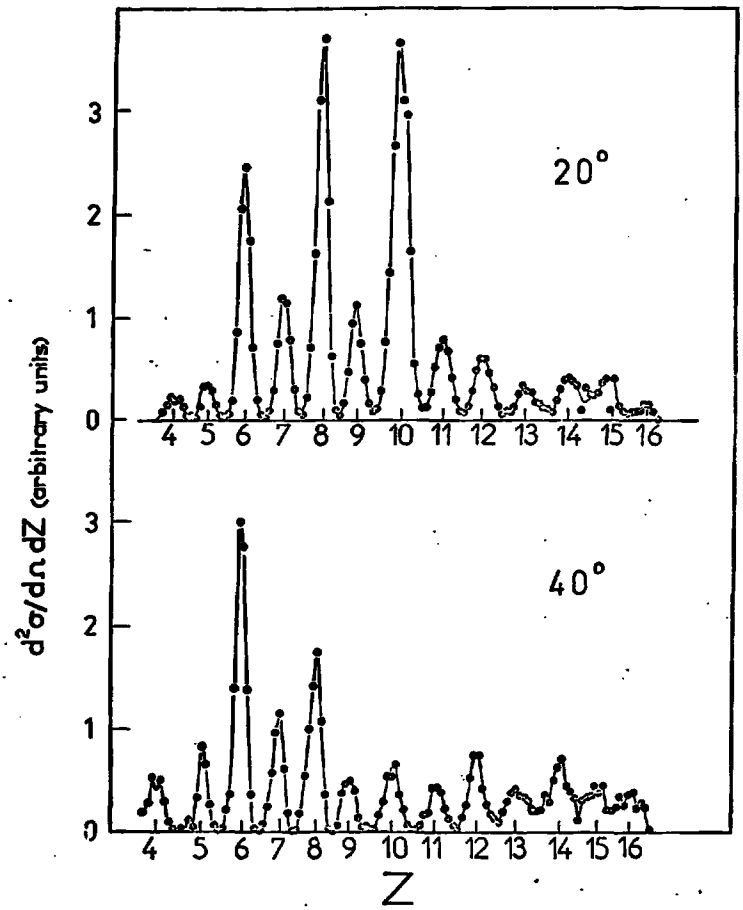
20°
40°
$d^2\sigma/d\Omega dZ$ (arbitrary units)
Z
0
1
2
3
4 5 6 7 8 9 10 11 12 13 14 15 16

FIG.1

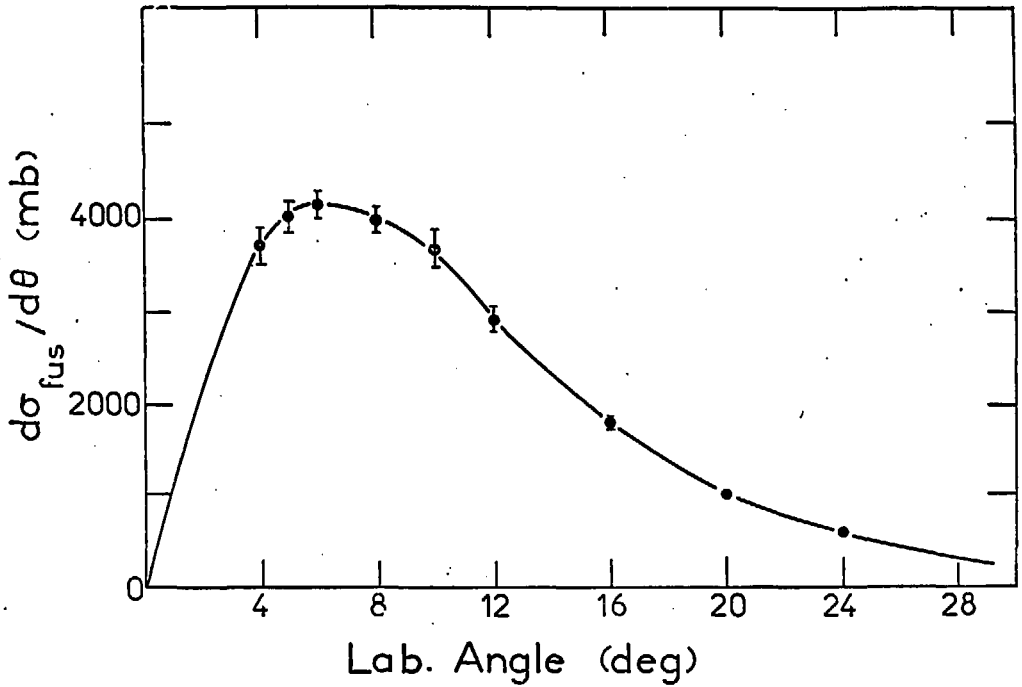

FIG. 2

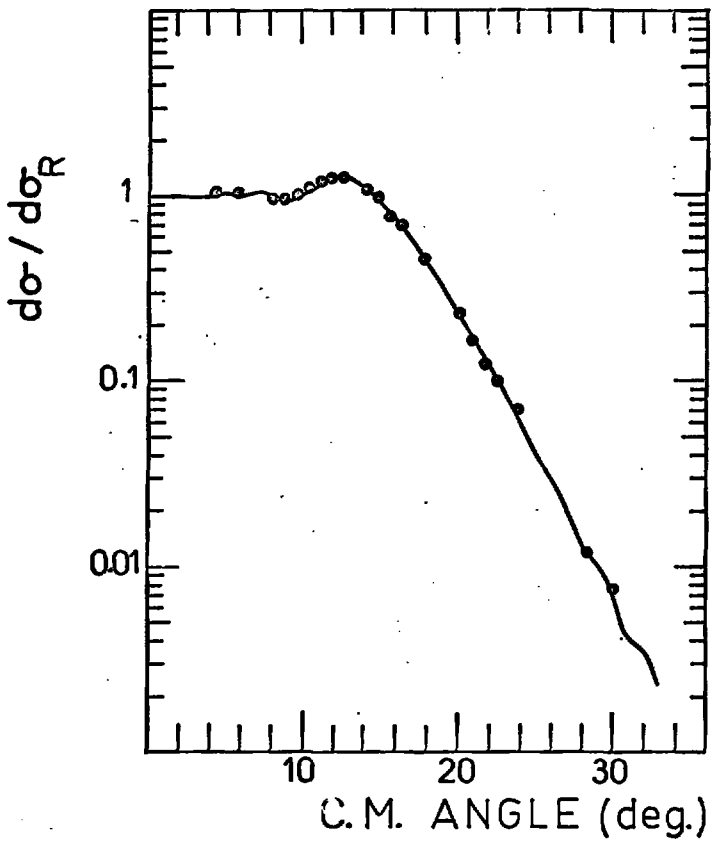

FIG. 3

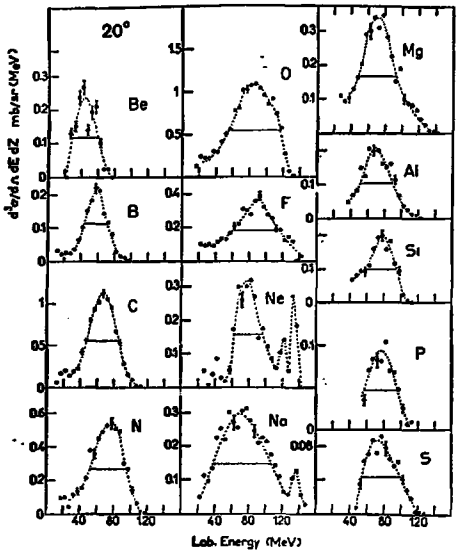
20°
Be
O
Mg
B
F
Al
C
Ne
Si
N
Na
P
S
d²σ/dΩdEdZ mb/sr·MeV
Lab. Energy (MeV)

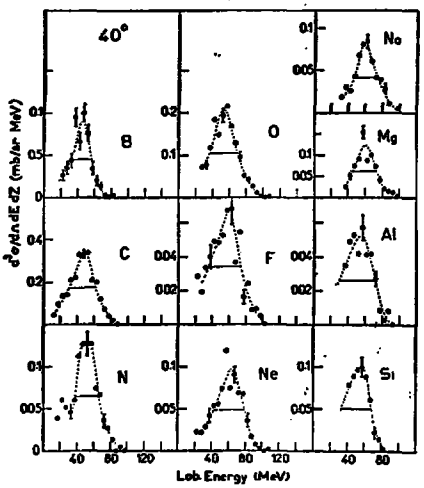
40°
B
O
Na
Mg
C
F
Al
N
Ne
Si
d²σ/dΩdEdZ (mb/sr· MeV)
Lab. Energy (MeV)

FIG.4

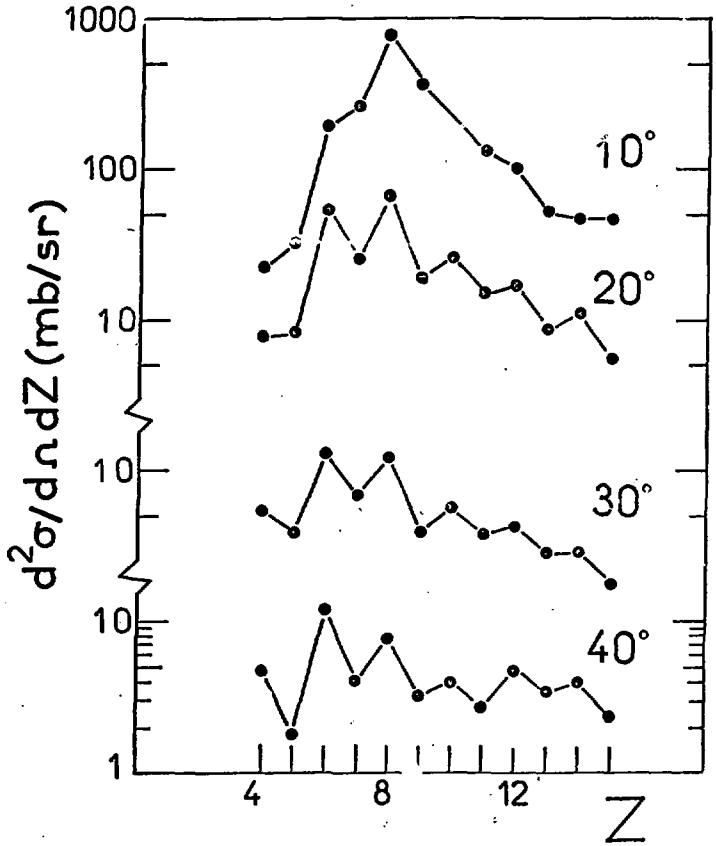

FIG. 5

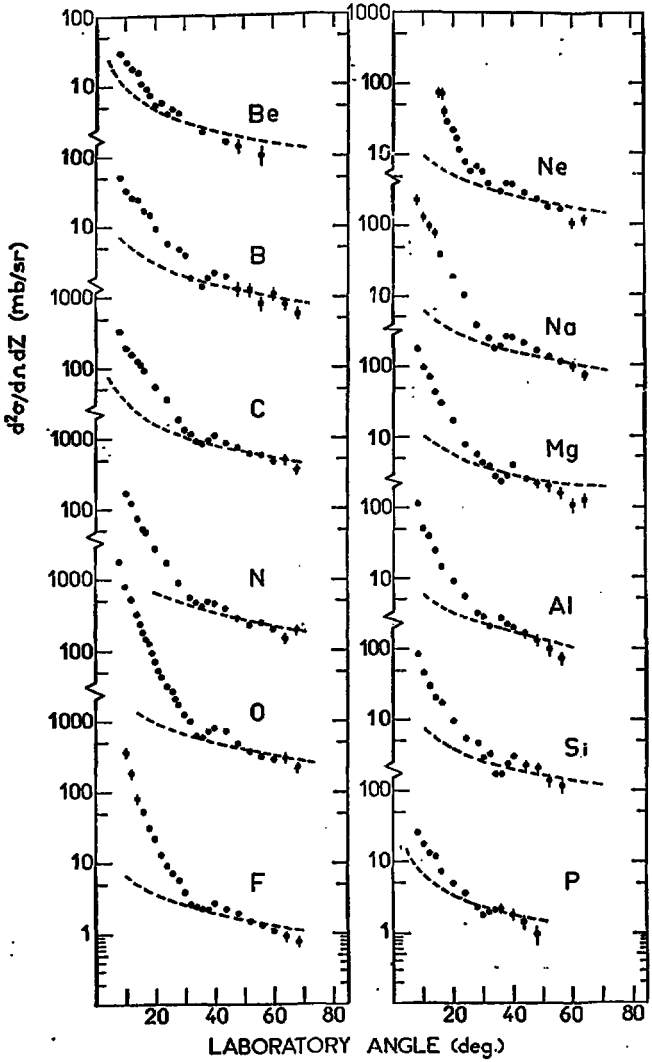
Be
B
C
N
O
F
Ne
Na
Mg
Al
Si
P
d²σ/dΩdZ (mb/sr)
LABORATORY ANGLE (deg.)
20
40
60
80

FIG. 6

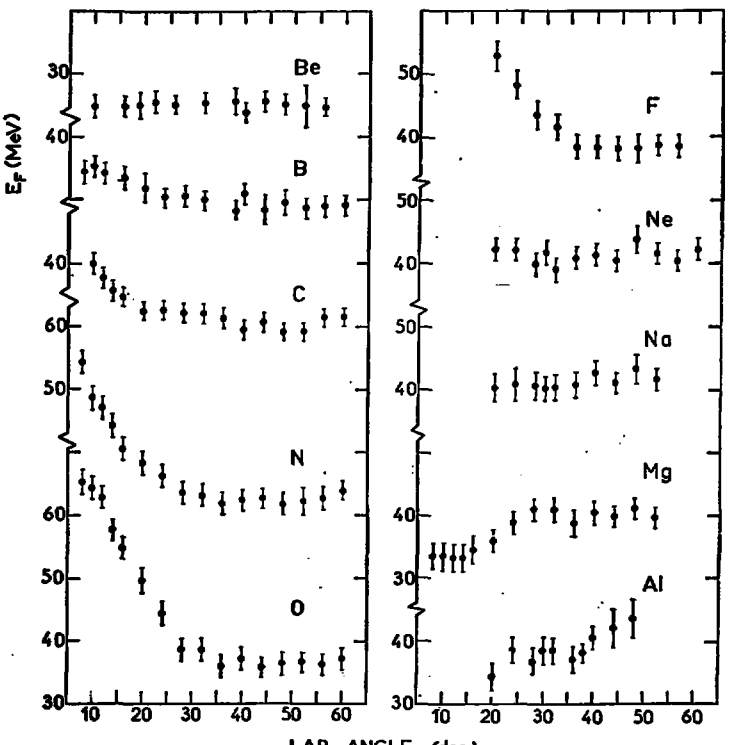

FIG.7

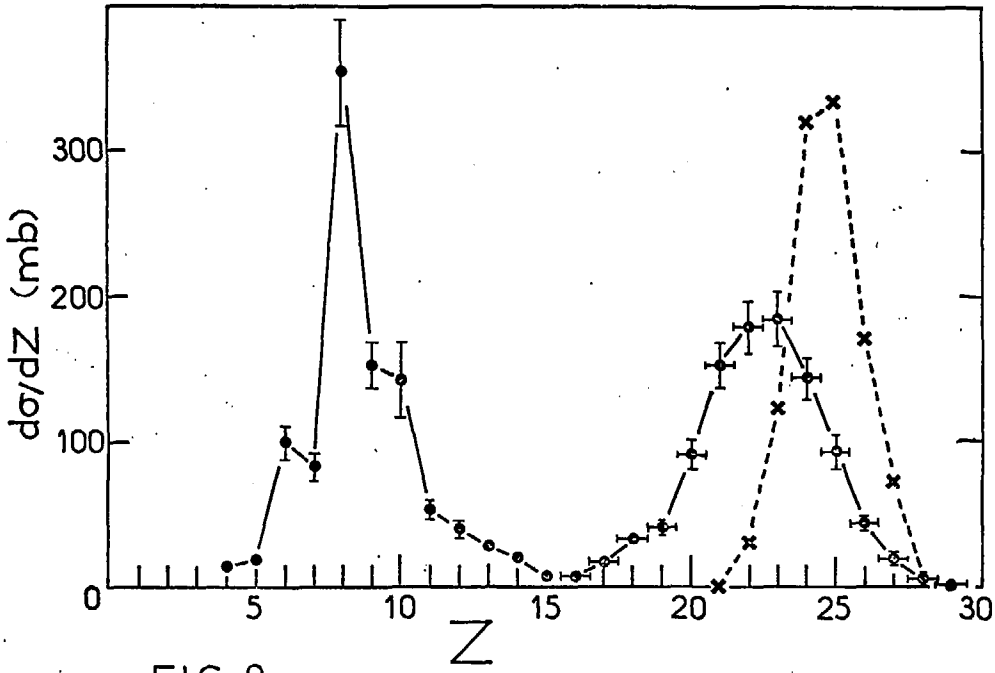

FIG. 8

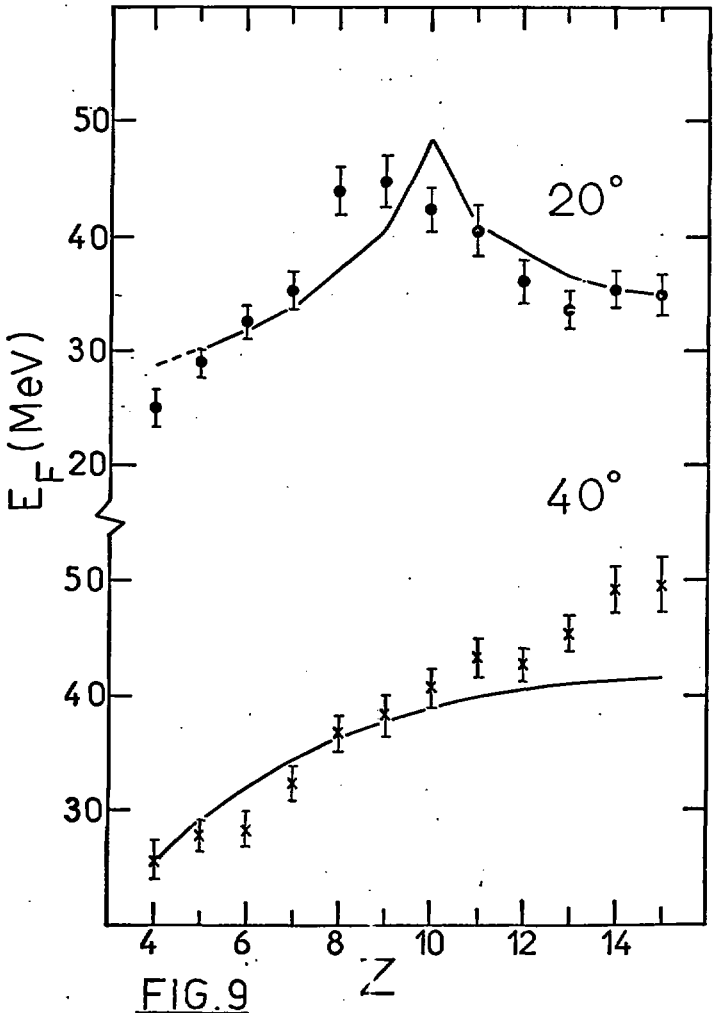

FIG.9